ARMA 19–xxx

SAND2019-2041C

Coupled hydro-mechanical modeling of injection-induced seismicity in the multiphase flow system

Chang, K.W.
Geotechnology & Engineering Department, Sandia National Laboratories, Albuquerque, NM, USA
Yoon, H.
Geomechanics Department, Sandia National Laboratories, Albuquerque, NM, USA
Martinez, M.J.
Engineering Sciences Center, Sandia National Laboratories, Albuquerque, NM, USA
Newell, P.
Department of Mechanical Engineering, The University of Utah, UT, USA

ABSTRACT: The fluid injection into the subsurface perturbs the states of pore pressure and stress on the pre-existing faults, potentially causing earthquakes. In the multiphase flow system, the contrast of fluid and rock properties between different structures produces the changes in pressure gradients and subsequently stress fields. Assuming two-phase fluid flow (gas-water system) and poroelasticity, we simulate the three-layered formation including a basement fault, in which injection-induced pressure encounters the fault directly given injection scenarios. The single-phase poroelasticity model with the same setting is also conducted to evaluate the multiphase flow effects on poroelastic response of the fault to gas injection. Sensitivity tests are performed by varying the fault permeability. The presence of gaseous phase reduces the pressure buildup within the highly gas-saturated region, causing less Coulomb stress changes, whereas capillarity increases the pore pressure within the gas-water mixed region. Even though the gaseous plume does not approach the fault, the poroelastic stressing can affect the fault stability, potentially the earthquake occurrence.

1. INTRODUCTION

The successful storage of carbon dioxide (CO_2) at commercial–scale requires to evaluate potentials of the seismic hazard and its affects on mechanical stability of the target formation [Verdon, 2013]. Injection-induced seismicity involves the mechanical stability of the pre-existing fault. Direct diffusion of pore pressure into the fault changes the effective stress on the fault, potentially causing earthquakes [Talwani, 1997, Zhang et al., 2013, Kerenan et al., 2014]. Considering coupling process between fluid flow and mechanical deformation, indirect stress transmission can disturb the stress state on the fault (called as "poroelastic stressing") without direct pore-pressure diffusion [Chang and Segall, 2016, Chang and Yoon, 2018].

Injection of CO_2 into brine aquifers generates the multiphase system where injected CO_2 (supercritical state) is more compressible and less dense than pre-existing brine at typical pressure and temperature of the reservoir. The difference of fluid properties will be an additional factor to cause variations in the spatio-temporal patterns of pore pressure and stress fields, ultimately seismic events.

The objective of this work is to understand the multiphase flow effects on injection-induced seismicity along the fault in a poroelasticity system. The perturbations in pore pressure and stress fields with variation in the fault permeability are examined from the comparative study of two- and single-phase flow systems. From the numerical results, we describe the physical mechanism of potential earthquakes on the fault in a coupled multiphase flow and poroelasticity system.

2. MODEL DESCRIPTION

2.1. Governing equations

In this study, we model two-phase fluid flow (gas and water) in a porous media. The dynamics of two-phase flow in a capillary porous medium is governed by the following equations [*Peaceman*, 1977]:

$$\frac{\partial(\rho_w \phi S_w)}{\partial t} = \nabla \cdot \left[\rho_w \frac{k k_{rw}}{\mu_w}(\nabla p_w - \rho_w \mathbf{g})\right] + Q_w \qquad (1)$$

Sandia National Laboratories is a multimission laboratory managed and operated by National Technology & Engineering Solutions of Sandia, LLC, a wholly owned subsidiary of Honeywell International Inc., for the U.S. Department of Energy's National Nuclear Security Administration under contract DE-NA0003525.

$$\frac{\partial(\rho_g \phi S_g)}{\partial t} = \nabla \cdot \left[\rho_g \frac{k k_{rg}}{\mu_g}\left(\nabla p_w + \nabla p_c - \rho_g g\right)\right] + Q_g \quad (2)$$

which represent mass conservation of water (subscript *w*, wetting phase) and supercritical CO_2 (subscript *g*, non-wetting phase), respectively. In these equations, ϕ is porosity, ρ_α is phase density ($\alpha = w$ or g), S_α is phase (fluid) saturation, k is the intrinsic permeability, μ_α is phase viscosity, **g** is gravity, and Q_α denotes mass sources, either external sources or inter-phase mass transfer between fluid phases. The two fluid phases are assumed to be immiscible, such that dissolution of CO_2 into water is neglected. The density and viscosity of CO_2 change with pressure (Figure 1), whereas water density is modeled as linear in pressure with compressibility of 3.6×10^{-10} [Pa^{-1}] and viscosity is assumed constant (μ_w = 0.75×10^{-3} [Pa·s]).

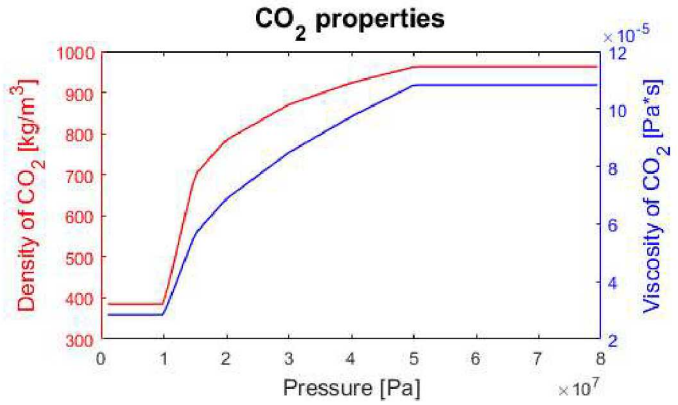

Fig. 1. Density and viscosity of CO_2 as a function of pressure at temperature T = 50°C.

We have also incorporated the Darcy flux terms (the terms in parenthesis on the right-hand-side), including pressure and gravitational forces, with the saturation dependent relative permeabilities, $k_{r\alpha}$ as well as capillary pressure $p_c = p_g - p_w$ defined by the van Genuchten function [van Genuchten, 1980]:

$$p_c = p_{ct}[(S_w^*)^{-1/m} - 1]^{1/n} \quad (3)$$

$$S_w^* = \frac{S_w - S_{wr}}{1 - S_{wr} - S_{gr}} \quad (4)$$

where p_{ct} is the entry capillary pressure (p_{ct} = 5 kPa for this study), n is the pore size distribution index ($n = 1/(1-m)$ = 1.57 for this study) and S_w^* is the normalized wetting phase saturation. $S_{\alpha r}$ is the residual saturation of each phase ($S_{\alpha r}$ = 0 for this study). The corresponding relative permeabilities are given by

$$k_{rw} = (S_w^*)^n \left[1 - \left(1 - S_w^{*\,1/m}\right)^m\right]^2 \quad (4)$$

$$k_{rg} = (1 - S_w^*)^n \left[1 - (S_w^*)^{1/m}\right]^{2m} \quad (5)$$

The pore space is assumed fully saturated with fluids, $S_w + S_g = 1$.

The solid mechanics is the quasi-static form of the linear momentum equation,

$$\nabla \cdot \boldsymbol{\sigma} + \rho \mathbf{g} = 0 \quad (6)$$

where $\boldsymbol{\sigma}$ is the Cauchy stress tensor, and ρ is bulk density of the mixture. Formulations of coupled deformation and flow in porous materials are based on the concept of effective stress in fluid-saturated porous media

$$\boldsymbol{\sigma}^{eff} = \boldsymbol{\sigma} + \alpha \mathbf{I} p \quad (7)$$

where α is the Biot parameter and p is the pore fluid pressure, often described as a saturation-weighted average of the phase pressures. For linear elastic isotropic material behavior, the stress-strain constitutive model is

$$\boldsymbol{\sigma}^{\text{eff}} = \lambda\, \text{trace}(\boldsymbol{\epsilon})\mathbf{I} + 2G\boldsymbol{\epsilon} \quad (8)$$

$$\boldsymbol{\epsilon} = \frac{1}{2}[\nabla \mathbf{u} + (\nabla \mathbf{u})^T] \quad (9)$$

where λ is the Lame coefficient ($\lambda = 2G\nu/(1-2\nu)$) is shear modulus, and the strain tensor ε is defined in terms of displacement **u**.

The appearance of the pore pressure term in the effective stress law explicitly displays coupling of the flow and mechanical deformation. In addition, deformations change porosity and permeability in the flow problem, computed via the deformation gradient from the solid mechanics problem. Owing to the dynamic deformation of the porous skeleton, flow and mechanics problems are computed on the deformed grid. Thus, treatments of large deformation problems with nonlinear constitutive models are implemented in this study.

2.2. Model domain

We model the two-dimensional (2-D) domain (2 km by 2 km) that represents the aerial view of the reservoir intersected by a basement fault. Supercritical CO_2 is uniformly injected into the center of the water-saturated reservoir (x_1, x_2) = (0,0) at the constant mass rate of 0.1 [kg/s] for 25 years. Initially the domain is at constant pressure ($p_0 = 0$) and fully saturated with water phase (S_w = 1). All boundaries have constant pressure ($p = p_0$) and water phase saturation ($S_w = 1 - S_{gr} = 1$) for drained conditions.

A strike-slip fault with the scale of 0.5 km (length) by 5 m (width) is located at 0.3 km away from the domain center is considered for the reference model. Assuming that the fault is critically stressed, small perturbations in the stress state on the fault can initiate fault slip,

potentially inducing seismicity. For the comparative study, the fault permeability (k_f) varies from 1×10^{-12} to 1×10^{-2} m^2 based on the field and laboratory measurement [IEAGHG, 2016]. All hydrogeological and mechanical parameter values for the reservoir and fault are listed in Table 2.

Table 2. Model properties: rock properties.

	Reservoir	Fault
Permeability, k [m^2]	1×10^{-15}	1×10^{-12}, 1×10^{-21}
Porosity, ϕ [–]	0.25	0.02
Poisson's ratio, ν [–]	0.2	0.2
Shear modulus, G [GPa]	10	6
Biot parameter, α [–]	0.267	0.62

The governing equations (1), (2), and (6) are numerically solved with initial and boundary conditions to study the perturbation in pore pressure and stress fields driven by fluid injection. The finite-element analysis is performed using Sierra/Aria module for multiphase flow and nonlinear geomechanics [Sierra Thermal/Fluid Development Team, 2018]. Rectangular elements are used for spatial discretization [Hughes, 2000], and a variable step method is employed for time integration [Dreij et al., 2011]. Mesh was highly refined near the boundaries of the faults and the injection point to resolve the strong pressure gradients. Note that coarse mesh in the fault zone may cause numerical diffusion that exaggerates the values of pore pressure and stresses over time.

2.3. Coulomb stress changes

The mechanical stability of the faults is effectively quantified by the Coulomb stress changes, defined in terms of the changes in stresses and pore pressure:

$$\Delta\tau = (\Delta\tau_s + f\Delta\sigma_n) + f\Delta p \qquad (10)$$

where $\Delta\tau_s$, $\Delta\sigma_n$, and Δp are the changes in shear and normal stresses, and pore pressure respectively from the initial state, and f is the friction coefficient. The positive values of each term imply that the fault failure is initiated under the critically stressed condition. Note that the first two terms evaluates the effect of mechanical deformation driven by the poroelastic coupling process [Chang and Segall, 2016]. Note that, without considering poroelasticity, the Eq. (10) is a function of the pore pressure change only ($\Delta\tau = f\Delta p$). Thus, the positive perturbation ($+\Delta\tau$) implies the initiation of the mechanical instability, potentially inducing earthquakes on the fault.

3. NUMERICAL RESULTS

The change in pore pressure and stresses plays a critical role in determining the fault stability associated with CO_2 injection. We model the single-phase flow model by injection water at the same mass rate to look into the multiphase flow effect (other parameters remain the same) in the poroelasticity system.

Figure 2 shows the spatial distribution of CO_2 saturation after 10 years with a contour of $\Delta p = 10$ MPa. CO_2 invades into the high-permeability fault and spread out along the fault (top figure) whereas pore pressure accumulates along the low-permeability fault, which slows down the CO_2 propagation in x-axis direction toward the fault (bottom figure).

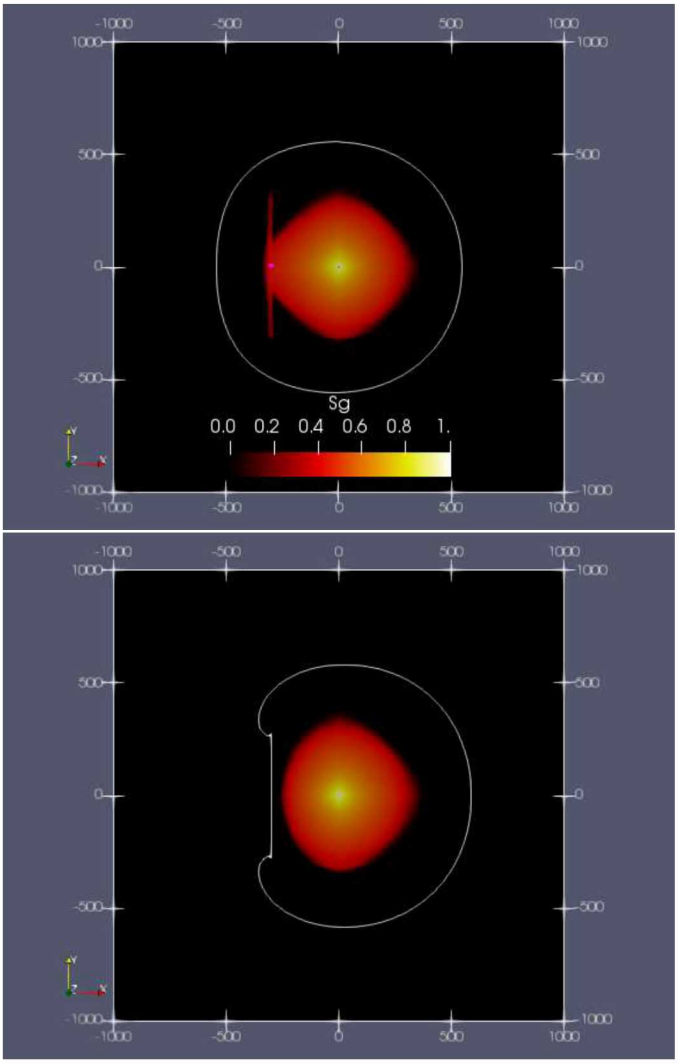

Fig. 2. Schematic description of the model domain. Refined numerical mesh is applied at the injection point and the fault zone to resolve strong gradients.

Figure 3 shows the spatial distribution of Δp along the center line in x-axis direction for conductive and sealing faults at $t = 10$ years. Near the injection well (highly CO_2-saturated region) experiences less pressure buildup due to larger mobility. As CO_2 plumes propagate, the gas-water mixed regions experience higher pore pressure.

For the high-permeability fault (top figure), pore pressure diffuses rapidly across the interface and spreads throughout the fault zone, which brings the equilibrium

state of the pressure field across the interface between the fault and neighboring reservoir. Note that the magnitude of the pressure increase depends on the injection operation (rate and period) and fault properties (geometry and hydraulic characteristics).

For the low-permeability fault (bottom figure), diffusion is impeded by lower permeability of the fault zone, acting as a hydraulic barrier. For both flow systems, the pressure accumulation is observed at the right-hand side of the fault near the injector. However, for the two-phase flow system, the water-wet fault and nearby formation act also as a capillary barrier formed by the large contrast in permeability across the interface between reservoir and fault. Note that the volume of shale in the fault plays a significant role in determining the capillary entry pressure (experimental study showed that shale volume of greater than 40% in the fault gives p_{ct} of 55 MPa [Lyon et al., 2005]). Larger capillary entry pressure requires pressure buildup sufficient to overcome the capillary barrier, potentially causing larger changes in Δp.

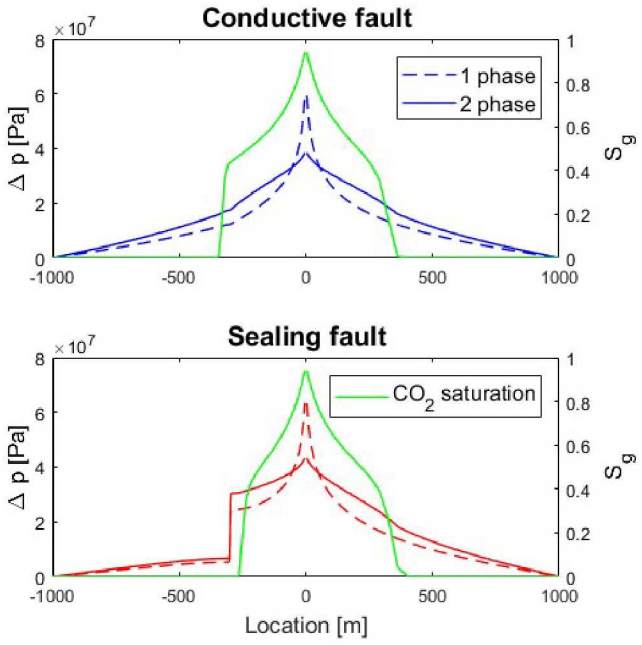

Fig. 3. Comparison of the temporal evolution of pore pressure at the center of the conductive and sealing faults (dashed and solid lines respectively) from two- and single-phase flow system (red and blue lines respectively)

In addition to the effect of the two-phase flow system on the mechanical stability of the formation, the poroelastic response to fluid injection also influences significantly the spatio-temporal perturbations in pore-pressure and stress fields. Poroelastic coupling effects on induced seismicity along the fault are quantified by pore pressure change ($f\Delta p$) and poroelastic stress change ($\Delta\tau_s + f\Delta\sigma_n$) [Chang and Segall, 2016].

Figure 4 shows the temporal distribution of $f\Delta p$, $\Delta\tau_s + f\Delta\sigma_n$, and $\Delta\tau$ in the middle of the fault.

Pore pressure increases rapidly in the high-permeability faults (blue lines in top figure). Once CO_2 plumes encounter the fault, capillary pressure generates larger $f\Delta p$. The low-permeability faults experience slower pore-pressure buildup due to low diffusivity (red lines in top figure).

CO_2 injection causes the reservoir bounding the fault expand, which generates compressional stresses within the fault zone (negative $\Delta\tau_s + f\Delta\sigma_n$). Within the high-permeability faults, rapid pressure buildup also generates strong compression as a poroelastic response of the rock solid for a relatively shorter period (blue lines in middle figure). On the other hand, within the low-permeability fault, slower increase in pore pressure and CO_2 plume propagation toward the fault generate gradual increase in compression (red lines in middle figure).

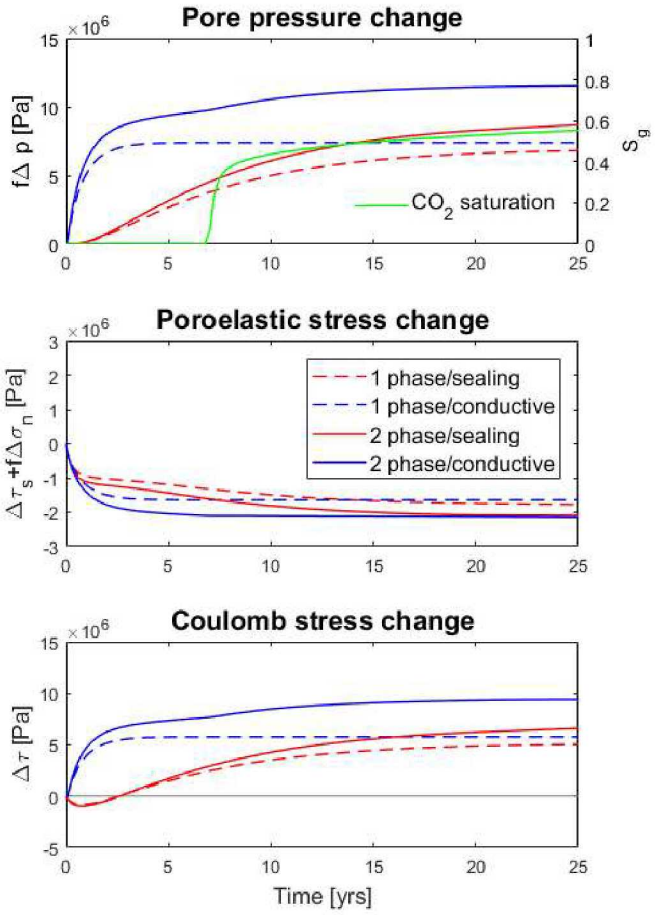

Fig. 4. Comparison of the pore-pressure distribution along the line (indicated by light blue at the sub-plot) for the conductive and sealing faults (top and bottom figures respectively) at t = 10 [yrs]. The injection well is located at x = 0 [m], and the fault location is indicated by a black dash line.

The summation of $f\Delta p$ and $\Delta\tau_s + f\Delta\sigma_n$ gives total Coulomb stress changes ($\Delta\tau$). The compressive poroelastic stresses reduces the direct impact of elevated pore pressure along the fault (comparison of top and

bottom figures). For the high-permeability fault, direct diffusion of pore pressure controls the fault stability substantially, generating positive $\Delta\tau$ during the whole injection period (blue lines). For the low-permeability fault, poroelastic stressing enhances the fault stability initially (generating negative $\Delta\tau$), and gradual pressure buildup destabilizes the fault over time (red lines).

4. CONCLUSIONS

Our numerical results show that multiphase flow in the poroelasticity system poses following effects on the potential of induced seismicity:

- Near the injection well, larger mobility of CO_2 phase reduces pressure buildup within the highly CO_2-saturated zone.
- Depending on the fault permeability, the fault can act as a hydraulic or capillary barrier against fluid phases, which can enhance the potential of induced seismicity along the fault.
- Poroelastic coupling can reduce the direct impact of pore-pressure buildup on the fault instability. The immediate mechanical response to CO_2 injection can enhance the stability of the low-permeability fault as a poroelastic response.

The uncoupled approach or single-phase flow system will not capture these physical mechanisms that can influence the fault stability, ultimately the occurrence of induced seismicity. Therefore, we suggest coupled modeling of the multiphase flow and poroelasticity system to predict important distinction in the spatio-temporal pattern of potential seismic events associated with geological CO_2 storage.

ACKNOWLEDGEMENTS

This work was supported by the Laboratory Directed Research and Development program at Sandia National Laboratories. Sandia National Laboratories is a multimission laboratory managed and operated by National Technology and Engineering Solutions of Sandia, LLC., a wholly owned subsidiary of Honeywell International, Inc., for the U.S. Department of Energy's National Nuclear Security Administration under contract DE-NA-0003525. This paper describes objective technical results and analysis. Any subjective views or opinions that might be expressed in the paper do not necessarily represent the views of the U.S. Department of Energy or the United States Government. No data was used in producing this manuscript.

REFERENCES

1. Verdon, J., J.-M. Kendall, A. Stork, R. Chadwick, D. White, and R. Bissell. 2013. Comparison of geomechanical deformation induced by megatonne-scale CO_2 storage at Sleipner, Weyburn, and In Salah, Proc. Natl. Acad. Sci., 110(30), E2762–E2771, doi:10.1073/pnas.13021561105.
2. Talwani, P. 1997. On the nature of reservoir-induced seismicity, Pure Appl. Geophys., 150(3-4), 473-492.
3. Zhang, Y., M. Person, J. Rupp, K. Elett, M. A. Celia, C. W. Gable, B. Bowen, J. Evans, L. Bandilla, P. Mozley, T. Dewers, and T. Elliot. 2013. Hydrogeologic controls on induced seismicity in crystalline basement rocks due to fluid injection into basal reservoirs, Ground Water, 51(4), 525–538, doi:10.1111/gwat.12071.
4. Kerenan, K. M., M. Weingarten, G. A. Abers, B. Bekins, and S. Ge. 2014. Sharp increase in central Oklahoma seismicity since 2008 induced by massive wastewater injection. Science 345, 448.
5. Chang, K. W., and P. Segall. 2016. Injection induced seismicity on basement faults including poroelastic stressing, J. Geophys. Res. Solid Earth, 121(4), 2708–2726, doi:10.1002/2015JB012561.
6. Chang, K. W. and H. Yoon. 2018. 3-D modeling of induced seismicity along multiple faults: Magnitude, rate, and location in a poroelasticity system, J. Geophys. Res. Solid Earth, 123(11), 9866-9883.
7. Peaceman, D.W. 1977. Fundamentals of Numerical Reservoir Simulation, Elsevier, New York.
8. Van Genuchten, M.T. 1980. A closed-form equation for predicting the hydraulic conductivity of unsaturated soils. Soil Sci. Soc. Am. J., 44, 892–898.
9. Sierra Thermal/Fluid Development Team. 2018. Sierra multimechanics module: Aria User Manual – Version 4.48, SAND2018-3717, Sandia National Laboratories, Albuquerque, NM.
10. Hughes, T.J.R. 2000. The Finite Element Method Linear Static and Dynamic Finite Element Analysis, Courier Dover Publ. Mineola, NY.
11. Dreij, K., Q.A. Chaudhry, B. Jernstrom, R. Morgenstern, and M. Hanke. 2011. A method for efficient calculation of diffusion and reactions of lipophilic compounds in complex cell geometry, PLoS One, 6(8), 1–18.
12. IEAGHG. 2016. Fault permeability, 2016/13.
13. Lyon, P. J., P. J. Boult, R. R. Hillis, and S. D. Mildren. 2005. Sealing by shale gouge and subsequent seal breach by reactivation: A case study of the Zema Prospect, Otway Basin, in P. Boult and J. Kaldi, eds., Evaluating fault and cap rock seals: AAPG Hedberg Series, no. 2 p. 179–197.